# Min-Cut Segmentation of Retinal OCT Images

Bashir Isa Dodo(✉), Yongmin Li, Khalid Eltayef, and Xiaohui Liu

Brunel University London, UB8 3PH London, UK
{Bashir.Dodo,Yongmin.Li,Khalid.Eltayef,XiaoHui.Liu}@brunel.ac.uk

**Abstract.** Optical Coherence Tomography (OCT) is one of the most vital tools for diagnosing and tracking progress of medication of various retinal disorders. Many methods have been proposed to aid with the analysis of retinal images due to the intricacy of retinal structures, the tediousness of manual segmentation and variation from different specialists. However image artifacts, in addition to inhomogeneity in pathological structures, remain a challenge, with negative influence on the performance of segmentation algorithms. In this paper we present an automatic retinal layer segmentation method, which comprises of fuzzy histogram hyperbolization and graph cut methods. We impose hard constraints to limit search region to sequentially segment 8 boundaries and 7 layers of the retina on 150 OCT B-Sans images, 50 each from the temporal, nasal and center of foveal regions. Our method shows positive results, with additional tolerance and adaptability to contour variance and pathological inconsistence of the retinal structures in all regions.

**Keywords:** Retinal layer segmentation · Optical Coherence Tomography · Graph-cut · Image analysis

## 1 Introduction

Segmentation using graph cut methods depends on the assignment of appropriate weight during graph construction. The paths obtained by the shortest path algorithms have no optimal way of handling inconsistencies (such as the irregularity in OCT images), as thus it sometimes obtains the wrong paths, which we call the "wrong short-cuts". To avoid the wrong short-cuts, we reassign the weights to promote the homogeneity between adjacent edges using fuzzy histogram hyperbolization. In other words, the edges with high value get higher weights, while those with low values become lower. The idea behind this weight reassignment is that, the transition between layers of OCT images which are from dark to light or vice versa are improved. This means we can better identify the layers by searching for the changes or transitions between layer boundaries. Additionally, we take into account the transition between the layers is in most cases very smooth, making it quite difficult to segment the layers. Now if we re-emphasize on this changes, such that they become clearer, this aids the algorithm in successful segmentation and avoiding wrong short-cuts.


A. Cliquet jr. et al. (Eds.): BIOSTEC 2018, CCIS 1024, pp. 86–99, 2019.
https://doi.org/10.1007/978-3-030-29196-9_5

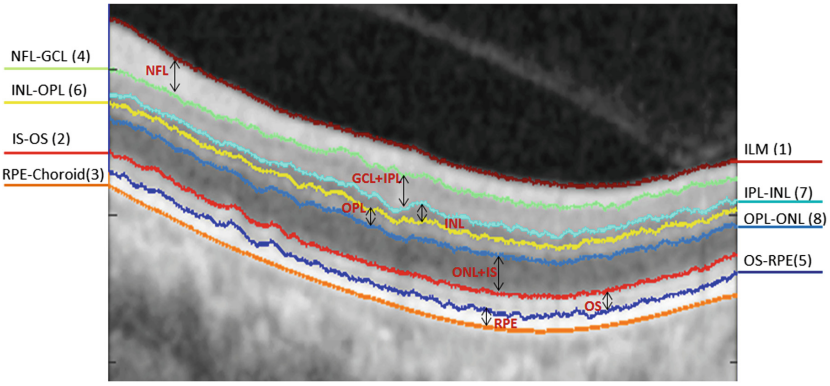


**Fig. 1.** Illustration of the 8 boundaries and 7 retinal layers segmented in the study. The numbers in brackets are the sequential order of the segmentation [8].

In this paper we take into account the effect of promoting continuity and discontinuity, in addition to adding hard constraints based on the structure of retina to segment 7 retinal layers including the Nerve Fibre Layer (NFL), the Ganglion Cell to Layer-Inner Plexiform Layer (GCL+IPL), the Inner Nuclear Layer (INL), the Outer Plexiform Layer (OPL), the Outer Nuclear Layer to Inner Segment (ONL+IS), the Outer Segment (OS) and the Retinal Pigment Epithelium (RPE) by detecting eight (8) layer boundaries. The locations of these layers and boundaries in an OCT image are illustrated in Fig. 1.

This paper is organized as follows. In Sect. 2, we review background information on the Graph-Cut segmentation method and the previous work in retinal layer segmentation. Section 3 describes the proposed segmentation method. Section 4 presents experimental results on 150 OCT images and finally conclusions are drawn in Sect. 5.

## 2 Background

### 2.1 The Graph-Cut Method

Graph-Cut is an optimization method that provides solution to many computational problems including image processing and computer vision as first reported by [23]. In the context of image processing, a graph $G$ is a pair $(\nu, \varepsilon)$ consisting of a node (referred to as Vertex in 3D nested grid) set $\nu$ and an edge set $\varepsilon \subset \nu$ x $\nu$. The source $s$ and the sink $t$ are the two main terminal nodes. The edge set comprises of two type of edges: the spatial edges $en = (r, q)$, where $r, q \in \nu \backslash \{s, t\}$, stick to the given grid and link two neighbor grid nodes r and q except $s$ and $t$; the terminal edges or data edges, i.e. $e_s = (s, r)$ or $e_t = (r, t)$, where $r \in \nu \backslash \{s, t\}$, link the specified terminal $s$ or $t$ to each grid node $p$ respectively. Each edge is assigned a cost $C(e)$, assuming all are non-negative i.e. $C(e) \geq 0$. A cut, also

known as the s-t cut, splits the image into two disjoint sets of $s$ and $t$. It partitions the spatial grid nodes of $\Omega$ into disjoint groups, whereby one belongs to source and the other belongs to the sink, such that

$$\nu = \nu_s \bigcup \nu_t, \nu_s \bigcap \nu_t = \emptyset \tag{1}$$

We then introduce the concept of max-flow/min-cut [10]. The max-flow calculates the maximum amount of flow allowed to pass from the source $s$ to the sink $t$ based on edges capacity, and is formulated by:

$$\max_{p_s} \sum_{v \in \nu \setminus \{s,t\}} p_s(v) \tag{2}$$

For each cut, the energy is defined as the sum of the costs C(e) of each edge e $\in \varepsilon_{st} \subset \varepsilon$, where its two end points belong to two different partitions. Hence the problem of min-cut is to find two partitions of nodes such that the corresponding cut-energy is minimal,

$$\min_{\varepsilon_{st} \subset \varepsilon} \sum_{e \in \varepsilon_{st}} C(e) \tag{3}$$

Additional insightful literature detailing the concept of graph-cut for image segmentation can be found in [4,15,29].

### 2.2 Segmentation of Retinal Layers

The segmentation of retinal layers has drawn a large number of researches, since the introduction of Optical Coherence Tomography (OCT) [13]. Manual segmentation of retinal OCT images is intricate and requires automated methods of analysis [1]. Various methods have been proposed to help with OCT image segmentation. In particular, the main discussions are on the number of layers, computational complexity, graph formulation and mostly now optimization and machine learning approaches. In this regard a multi-step approach was developed by [2]. However the results obtained were highly dependent on the quality of images and the alterations induced by retinal pathologies. A 1-D edge detection algorithm using the Markov Boundary Model [16], which was later extended by [3] to obtain the optic nerve head and RNFL. Seven layers were obtained by [5] using a peak search interactive boundary detection algorithm based on local coherence information of the retinal structure. The Level Set method was used by [19,26–28] which were computationally expensive compared to other optimization methods. Graph based methods in [11,12,20–22] have reported successful segmentation results, with varying success rates. Recently, [9] proposed a method using the Fuzzy Histogram Hyperbolization (FHH) to improve the image quality, then embedded the image into the continuous max-flow to simultaneously segment 4 retinal layers.

In recent years, researchers have been inquisitive on the use of gradient information derived from the retinal structures. This information has been utilised

with the Graph-Cut method, where the retinal architecture and dynamic programming were deployed to limit the search space and reduce computational time respectively [6]. This method was recently extended to the 3D volumetric analysis by [24] in OCTRIMA 3D with edge map and convolution kernel in addition to hard constraints in calculating weights. The OCTRIMA 3D approach also exploited spatial dependency between adjacent frames to reduce processing time. Combination of methods including Edge detection and polynomial fitting [18] and machine learning with random forest classifier [17] were yet other approaches proposed to obtain the retinal layers from gradient information. The use of OCT gradient information is primarily due to the transition that occurs in the vertical direction at each layer boundary, thereby attracting segmentation algorithms to exploit this advantage. Our method takes into account the retinal structure and gradient information, but more importantly, the re-assignment of weights in the adjacency matrix is paramount to the success of our graph-cut approach.

## 3 The Proposed Method

In this section we explain the components of our approach to segmenting 8 retinal layer boundaries from OCT B-Scan images. A schematic representation of these components is illustrated in Fig. 2.

### 3.1 Pre-processing

Like most medical images, OCT suffer from a granular pattern called speckle noise. This noise is very common in OCT images, which has negative effects on further processing, for example, the retinal OCT images have low Signal to Noise Ratio (SNR) due to the strong amplitude of speckle noise. Various methods have been used to handle the presence of noise. In this work, we pre-process the images with a Gaussian filter to suppress the speckle noise and enhance the retinal layer boundaries, which is important for the weight calculation in the next stage. This also reduces false positive in the segmentation stage. An example of a pre-processed image compared to its original is shown in Fig. 3.

### 3.2 Graph Formulation

In this stage we obtain the vertical gradient of the image, normalize the gradient image to values in the range of 0 to 1, and then obtain the inverse of the normalized image gradient. Example of the gradient images are shown in Fig. 4. The two normalized gradient images are then used to obtain two separate undirected adjacency matrices, where Fig. 4(left) contains information of light-dark transitions while Fig. 4(right) contains information for transition from dark-light. The adjacency matrices are formulated with the following equation adapted from [6]:

$$w_{ab} = 2 - g_a - g_b + w_{min} \tag{4}$$

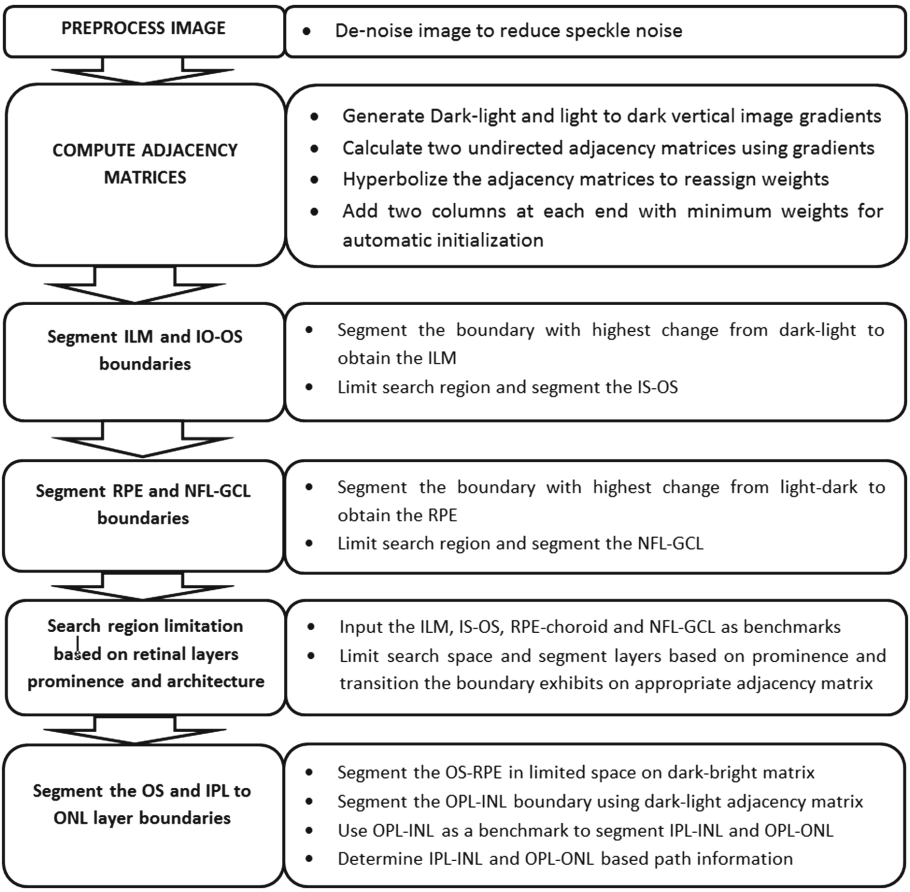


**Fig. 2.** Main steps of segmentation algorithm schematic representation [8].

where $w_{ab}$, $g_a$, $g_b$ and $w_{min}$ are the weights assigned to the edge connecting any two adjacent nodes $a$ and $b$, the vertical gradient of the image at node $a$, the vertical gradient of the image at node $b$, and the minimum weight added for system stabilization. To improve the continuity and homogeneity in the adjacency matrices they are hyperbolized, firstly by calculating the membership function with the fuzzy sets Eq. (5) [25] and then transformed with Eq. (6).

$$w'_{ab} = \frac{w_{ab} - w_{mn}}{w_{mx} - w_{mn}}. \tag{5}$$

where $w_{mn}$ and $w_{mx}$ represents the maximum and minimum values of the adjacency matrix respectively. The adjacency matrices are then transformed with the following equation:

$$w''_{ab} = (w'_{ab})^{\beta} \tag{6}$$

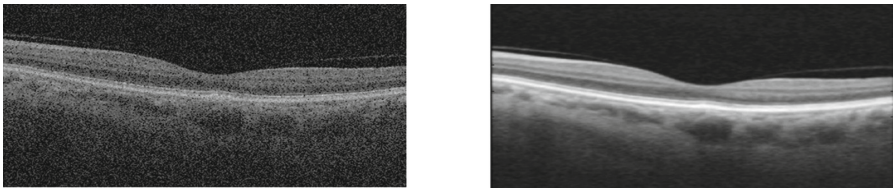

**Fig. 3.** Image pre-processing: original image corrupted with speckle noise (left) compared to filtered image by Gaussian (right) [8].

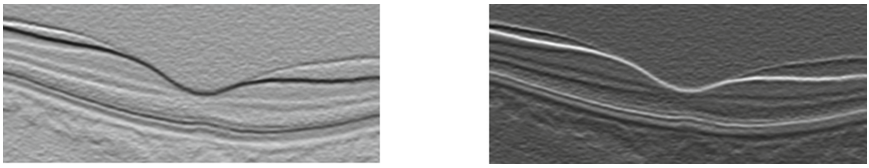

**Fig. 4.** Image gradients used in generating dark-bright adjacency matrix (left) and bright-dark adjacency matrix (right) [8].

where $w'_{ab}$ is the membership value from (5), and $\beta$, the fuzzifier is a constant. Considering the number of edges in an adjacency matrix, we use a constant $\beta$ instead of calculating the fuzziness. The main reason is to reduce computational time and memory usage. The resulting adjacency matrices are such that we reassign the weights, and the edges with high weights get higher values while those with low values get lower edge weights. Our motive here is that if we re-emphasize continuity or discontinuity, the algorithm would perform better, wherein our method we improve both by transforming the matrices. The region of the layers get similar values, while that of the background gets lower along the way. This is more realistic and applicable in this context (as the shortest path is greedy search approach), because at the boundary of each layer there is a transition from bright to dark or dark to bright, and therefore improving it aids the algorithm in finding correct optimal solutions that are very close to the actual features of interest.

The weight calculation is followed by several sequential steps of segmentation that we discuss in the next few subsections. We adopt layer initialization from [6], where two columns are added to either side of the image with minimum weights ($w_{min}$), to enable the cut move freely in those columns. We base this initialization from the understanding that each layer spans horizontally across the image, and that the graph-cut method prefers paths with minimum weights. We utilize the Djikstra's algorithm [7] in finding the minimum weighted path in the graph, which corresponds to layer boundaries. To segment multiple regions, we use an iterative search in limited space because graph-Cut methods are optimal at finding one boundary at a time. Limiting the region of search is a complex task, it requires prior knowledge and is dependent on the structure of the features or

regions of interest. More information on automatic layer initialization and region limitation can be obtained from [6,14].

### 3.3 ILM and IS-OS Segmentation

It is commonly accepted that the NFL, IS-OS and RPE exhibit high reflectivity in an OCT image [6,18,24]. Taking this reflectivity and the dark-bright adjacency matrix into account, we identify the ILM and IS-OS boundaries using Dijkstra's algorithm [7]. More specifically, the ILM (vitreous-NFL) boundary is segmented by searching for the highest change from dark to light, and this is because there is a sharp change in the transition. Additionally, it is amidst extraneous features, above it is the background region in addition to no interruption of the blood vessels, as can be seen in the gradient image in Fig. 4(right). All of the above reasons make it easier to segment the ILM than other layers. To segment the IS-OS boundary, We limit the search region below ILM for the next highest change from dark-bright. We then use the mean value of the vertical axis of the paths obtained, as a precaution to confirm which layer was segmented, because the ILM is above the IS-OS take (similar to [6]).

### 3.4 RPE and NFL-GCL Segmentation

As mentioned in the previous subsection, RPE is one of the most reflective layers. The RPE-Choroid boundary exhibits the highest bright-dark layer transition as can be seen in Fig. 4(left). Besides, it is better to search for the transition from bright-dark for the RPE based on experimental results, interference of blood vessels and the disruption of hyper-reflective pixels in the choroid region. Therefore searching for the highest bright-dark transition is ideal for the RPE most especially to adapt to noisy images. Now to segment the NFL-GCL boundary we limit the search space between ILM to IS-OS and utilize the bright-dark adjacency matrix to find the minimum weighted path. The resulting path is the NFL-GCL boundary, as it is one of the most hyper-reflective layers. Furthermore, the NFL-GCL and IS-OS boundaries exhibit the second highest bright-dark and dark-bright transition respectively in an OCT image. If we limit our search space to regions below the ILM and above the RPE, the resulting bright-dark and dark-bright minimum paths are the NFL-GCL and IS-OS respectively. It is also significant to note we use the paths obtained from one adjacency matrix to limit the region on either of the matrices. This is feasible because the paths are $(x, y)$ coordinates and the matrices are of the same size. For example, in finding the NFL-GCL boundary on the bright-dark adjacency matrix, we use paths of the ILM and IS-OS obtained from the dark-bright matrix to limit the search region.

### 3.5 OS and IPL to ONL Segmentation

Now that we have segmented the most prominent boundaries, we use them as benchmarks to limit the search space in order to segment the OS-RPE, IPL-INL,

INL-OPL, and OPL-ONL. We obtain the OS-RPE boundary by searching for the dark-bright shortest path between IS-OS and the RPE-Choroid. As for the remaining boundaries, we first segment the INL-OPL by searching for the shortest path between NFL-GCL and IS-OS on the dark-bright adjacency matrix, primarily because it exhibits a different transition from the IPL-INL and OPL-ONL boundaries. Consequently, the IPL-INL and OPL-ONL boundaries are obtained by limiting the region of path search between INL-OPL and NFL-GCL, and INL-OPL and IS-OS regions respectively, on the bright-dark adjacency matrix.

### 3.6 Avoiding the Cortical Vitreous

The vitreous cortex depicts a layer-like structure, just above the ILM, which lures the algorithm into finding unintended boundaries as illustrated in Fig. 5. To handle this issue, we impose a hard constraint to restrict all paths between the ILM to RPE boundaries inclusive. This is because the ILM exhibits the highest transition from dark-bright, while the RPE exhibits the highest transition from bright-dark. This helps the algorithm in avoiding features that imitate the retinal structures.

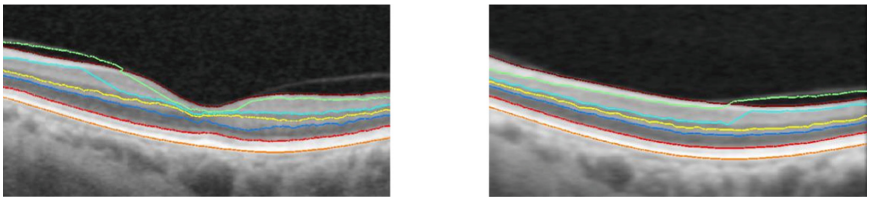

**Fig. 5.** Error in segmentation caused by vitreous cortex at temporal region (left) and Nasal region (right).

## 4 Experimental Results

The performance evaluation of our proposed method was tested on a dataset of 150 B-scan OCT images centred on the macular region. The data was collected in Tongren Hospital with a standard imaging protocol for retinal diseases such as glaucoma. Each B-scan image has a resolution of 512 pixels in depth and 992 pixels across section with 16 bits per pixel. Prior to segmenting the images, we cropped 15% percent of the image height from the top to remove regions with low signal and no features of interest. The ground truth images used in our experiments were manually labeled under the supervision of clinical experts. We segment seven retinal layers automatically using MATLAB 2016a software. Using a computer with Intel i5-4590 CPU, clock of 3.3 GHz, and 8 GB RAM memory, the average computational time was 4.25 s per image. The method obtains the boundaries in the order from ILM(Vitreous-NFL), IS-OS, RPE-Choroid, NFL-GCL, OS-RPE, INL-OPL, IPL-INL to OPL-ONL respectively. The locations of

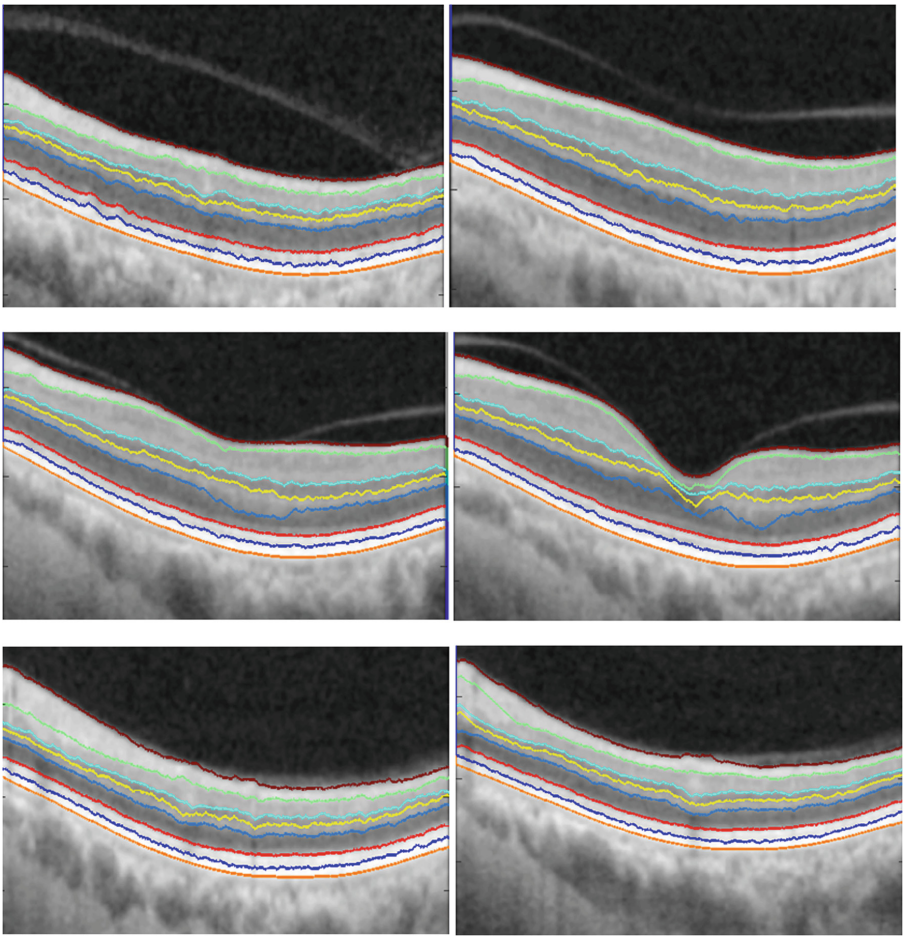

**Fig. 6.** Segmentation results of 8 boundaries and 7 layers. Boundaries from top to bottom, the segmented boundaries are ILM, NFL-GCL, IPL-INL, INL-OPL, OPL-ONL, IS-OS, OS-RPE and RPE-Choroid [8].

these boundaries and the sequential segmentation order of the 8 retinal layer boundaries and underlying 7 layers were shown earlier in Fig. 1, and we show output sample of results achieved in Fig. 6.

To evaluate the proposed method we calculate the Root Mean Squared Error (RMSE), and Mean Absolute Deviation (MAD) by (7). Table 1 shows output of the mean and standard deviation of both MAD and RMSE, for the seven layers targeted in this study.

$$
\begin{aligned}
&MAD(GT, SEG) = \\
&0.5 * \left( \frac{1}{n} \sum_{i=1}^{n} d(pt_i, SEG) + \frac{1}{m} \sum_{i=1}^{m} d(ps_i, GT) \right) \\
&RMSE = \sqrt{\frac{1}{n} \sum_{i=1}^{n} (SEG_i - GT_i)^2} \\
&Dice \qquad\qquad = \frac{2 \mid GT_i \cap SEG_i \mid}{\mid GT_i \mid + \mid SEG_i \mid}
\end{aligned}
\tag{7}
$$

where $SEG_i$ is the pixel labelled as retinal Layer (foreground) by the proposed segmentation method and $GT_i$ is the true retinal layers pixel in the manually annotated image (ground truth) image. In computing the MAD $pt_i$ and $ps_i$ represent the coordinates of the images, while $d(pt_i, SEG)$ is the distance of $pt_i$ to the closest pixel on $SEG$ with the same segmentation label, and $d(ps_i, GT)$ is the distance of $ps_i$ to the closest pixel on $GT$ with the same segmentation label. $n$ and $m$ are the number of points on $SEG$ and $GT$ respectively. For all layers our method has performed well. Especially considering the low value of NFL for both MAD and RMSE. The high value in ONL+IS is due to the presence of high noise and lower reflectivity of the boundaries within the region, however, this is still considerably low.

**Table 1.** Performance evaluation: Mean and Standard Deviation (STD) of RMSE and MAD for 7 retinal layers on 150 SD-OCT B-Scan images (Units in pixels) [8].

| *RetinalLayer* | *MeanMAD* | *MeanRMSE* | *STDMAD* | *STDRMSE* |
|---|---|---|---|---|
| NFL | 0.2689 | 0.0168 | 0.0189 | 0.0121 |
| GCL+IPL | 0.5938 | 0.0432 | 0.0592 | 0.0382 |
| INL | 0.6519 | 0.0387 | 0.0792 | 0.0612 |
| OPL | 0.5101 | 0.0446 | 0.0410 | 0.0335 |
| ONL+IS | 0.6896 | 0.0597 | 0.0865 | 0.0329 |
| OS | 0.4617 | 0.0341 | 0.0360 | 0.0150 |
| RPE | 0.4617 | 0.0341 | 0.0360 | 0.0150 |

Furthermore, The retinal nerve fibre layer thickness (RNFLT), the area between ILM and NFL-GCL, is critical in diagnosing ocular diseases, including glaucoma. For this reason, we evaluated the RNFLT with four additional criteria, namely, accuracy, sensitivity (true positive rate (TPR)), error rate (FPR) and the Dice index (coefficient). These measurements are computed with the

**Table 2.** Mean for accuracy, sensitivity, error rate and Dice coefficient of the Retinal Nerve Fibre Layer Thickness (RNFLT) and their respective standard deviation (STD). [8].

| *Criteria* | *Mean* | *STD* |
|---|---|---|
| Accuracy | 0.9816 | 0.0375 |
| Sensitivity | 0.9687 | 0.0473 |
| Error Rate | 0.0669 | 0.0768 |
| Dice | 0.9746 | 0.0559 |

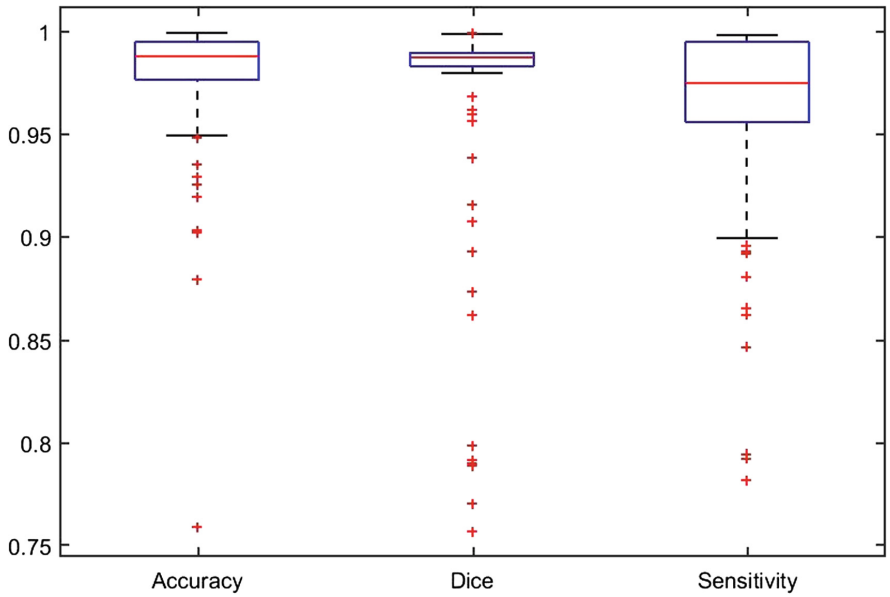


**Fig. 7.** Box plot for values distribution of Accuracy, Dice coefficient and Sensitivity of RNFLT from Table 2.

following equations while the Dice is computed from (7):

$$\begin{aligned} Accuracy &= \frac{TP+TN}{(TP+FP+FN+TN)} \\ Sensitivity(TPR) &= \frac{TP}{(TP+FN)} \\ ErrorRate(FPR) &= \frac{FP}{(FP+TN)} \end{aligned} \tag{8}$$

where $TP$, $TN$, $FP$ and $FN$ refers to true positive, true negative, false positive and false negative respectively. Distinctively, $TP$ represents the number of pixels which are part of the region that are labeled correctly by both the method and

the ground truth. $TN$ represents the number of pixels which are part of the background region and labeled correctly by both the method and the ground truth. $FP$ represents the number of pixels labeled as a part of the region by the method but labeled as a part of the background by the ground truth. Finally, $FN$ represents the number of pixels labeled as a part of the background by the system but labeled as a part of the region in ground truth. The Mean and standard Deviation of applying the above criteria on the achieved results for the RNFLT are shown in Table 2, and the distribution of these values in Fig. 7.

Some of the facts we draw from the results in Table 2 and their distribution Fig. 7 are as follows:

1. The method achieves more than 95% accuracy in most images
2. The method obtain paths very close to the actual retinal boundaries by achieving mean sensitivity of ≈97% over 150 images, which portrays adaptability to contours of the retinal layers.
3. The distribution of the dice score in Fig. 7 further attests to the statements in 2 above, i.e there is high overlap between the manual annotation and results obtained by our method.

## 5 Conclusions

We have presented a comprehensive approach towards retinal OCT image analysis. Our fully automatic method is capable of segmenting 7 retinal layers across 8 layer boundaries. The core of the method is the integration of the adjacency matrices from vertical gradients with improved weight calculation into a sequential process of the Graph-Cut framework using Dijkstra's algorithm [7]. Categorically, the sequential segmentation process is based on the unique characteristics of reflectivity of different retinal layers and their transitions at the boundaries. We have applied the proposed method to a dataset of 150 OCT B-scan images, with successful segmentation results. Additionally, quantitative evaluation indicates that the segmentation measurement is very close to the ground-truth. Furthermore, it is evident prior knowledge plays an essential role in segmentation. Therefore studies on how to automatically derive this information from images and electronic health records will be necessary because this information can be useful in optimizing image analysis algorithms, particularly methods of statistical based modelling.

## References

1. Baglietto, S., Kepiro, I.E., Hilgen, G., Sernagor, E., Murino, V., Sona, D.: Segmentation of retinal ganglion cells from fluorescent microscopy imaging. In: Proceedings of the 10th International Joint Conference on Biomedical Engineering Systems and Technologies (BIOSTEC 2017), pp. 17–23 (2017). https://doi.org/10.5220/0006110300170023

2. Baroni, M., Fortunato, P., La Torre, A.: Towards quantitative analysis of retinal features in optical coherence tomography. Med. Eng. Phys. **29**(4), 432–441 (2007). https://doi.org/10.1016/j.medengphy.2006.06.003
3. Boyer, K.L., Herzog, A., Roberts, C.: Automatic recovery of the optic nervehead geometry in optical coherence tomography. IEEE Trans. Med. Imaging **25**(5), 553–570 (2006). https://doi.org/10.1109/TMI.2006.871417
4. Boykov, Y., Jolly, M.P.: Interactive graph cuts for optimal boundary & region segmentation of objects in N-D images. In: Proceedings Eighth IEEE International Conference on Computer Vision, ICCV 2001, vol. 1(July), pp. 105–112 (2001). https://doi.org/10.1109/ICCV.2001.937505
5. Cabrera Fernández, D., Salinas, H.M., Puliafito, C.A.: Automated detection of retinal layer structures on optical coherence tomography images. Opt. Express **13**(25), 10200 (2005). https://doi.org/10.1364/OPEX.13.010200
6. Chiu, S.J., Li, X.T., Nicholas, P., Toth, C.A., Izatt, J.A., Farsiu, S.: Automatic segmentation of seven retinal layers in SDOCT images congruent with expert manual segmentation. Opt. Express **18**(18), 19413–19428 (2010). https://doi.org/10.1364/OE.18.019413
7. Dijkstra, E.W.: A note on two problems in connexion with graphs. Numer. Math. **1**(1), 269–271 (1959)
8. Dodo, B.I., Li, Y., Eltayef, K., Liu, X.: Graph-cut segmentation of retinal layers from OCT images. In: Proceedings of the 11th International Joint Conference on Biomedical Engineering Systems and Technologies. BIOIMAGING, vol. 2, pp. 35–42. INSTICC, SciTePress (2018). https://doi.org/10.5220/0006580600350042
9. Dodo, B.I., Li, Y., Liu, X.: Retinal OCT image segmentation using fuzzy histogram hyperbolization and continuous max-flow. In: 2017 IEEE 30th International Symposium on Computer-Based Medical Systems (CBMS), pp. 745–750. IEEE (2017)
10. Ford, L.R., Fulkerson, D.R.: Maximal flow through a network. J. Can. de mathématiques **8**, 399–404 (1956). https://doi.org/10.4153/CJM-1956-045-5
11. Garvin, M.K., Abràmoff, M.D., Wu, X., Russell, S.R., Burns, T.L., Sonka, M.: Automated 3-D intraretinal layer segmentation of macular spectral-domain optical coherence tomography images. IEEE Trans. Med. Imaging **28**(9), 1436–1447 (2009). https://doi.org/10.1109/TMI.2009.2016958
12. Haeker, M., Wu, X., Abràmoff, M., Kardon, R., Sonka, M.: Incorporation of regional information in optimal 3-D graph search with application for intraretinal layer segmentation of optical coherence tomography images. In: Karssemeijer, N., Lelieveldt, B. (eds.) IPMI 2007. LNCS, vol. 4584, pp. 607–618. Springer, Heidelberg (2007). https://doi.org/10.1007/978-3-540-73273-0_50
13. Huang, D., et al.: Optical coherence tomography. Sci. (New York, N.Y.) **254**(5035), 1178–1181 (1991). https://doi.org/10.1126/science.1957169
14. Kaba, D., et al.: Retina layer segmentation using kernel graph cuts and continuous max-flow. Opt. Express **23**(6), 7366–7384 (2015). https://doi.org/10.1364/OE.23.007366
15. Kolmogorov, V., Zabih, R.: What energy functions can be minimized via graph cuts? IEEE Trans. Pattern Anal. Mach. Intell. **26**(2), 147–159 (2004). https://doi.org/10.1109/TPAMI.2004.1262177
16. Koozekanani, D., Boyer, K., Roberts, C.: Retinal thickness measurements from optical coherence tomography using a Markov boundary model. IEEE Trans. Med. Imaging **20**(9), 900–916 (2001). https://doi.org/10.1109/42.952728
17. Lang, A., et al.: Retinal layer segmentation of macular OCT images using boundary classification. Biomed. Opt. Express **4**(7), 1133–1152 (2013). https://doi.org/10.1364/BOE.4.001133

18. Lu, S., Yim-liu, C., Lim, J.H., Leung, C.K.S., Wong, T.Y.: Automated layer segmentation of optical coherence tomography images. In: Proceedings - 2011 4th International Conference on Biomedical Engineering and Informatics, BMEI 2011, vol. 1, no. 10, pp. 142–146 (2011). https://doi.org/10.1109/BMEI.2011.6098329
19. Novosel, J., Vermeer, K.A., Thepass, G., Lemij, H.G., Vliet, L.J.V.: Loosely coupled level sets for retinal layer segmentation in optical coherence tomography. In: IEEE 10th International Symposium on Biomedical Imaging, pp. 998–1001 (2013)
20. Salazar-Gonzalez, A., Kaba, D., Li, Y., Liu, X.: Segmentation of the blood vessels and optic disk in retinal images. IEEE J. Biomed. Health Inform. **18**(6), 1874–1886 (2014)
21. Salazar-Gonzalez, A., Li, Y., Liu, X.: Automatic graph cut based segmentation of retinal optic disc by incorporating blood vessel compensation. J. Artif. Intell. Soft Comput. Res. **2**(3), 235–245 (2012)
22. Salazar-Gonzalez, A.G., Li, Y., Liu, X.: Retinal blood vessel segmentation via graph cut. In: International Conference on Control Automation Robotics and Vision, pp. 225–230 (2010)
23. Seheult, A., Greig, D., Porteous, B.: Exact maximum a posteriori estimation for binary images. J. R. Stat. Soc. **51**(2), 271–279 (1989)
24. Tian, J., Varga, B., Somfai, G.M., Lee, W.H., Smiddy, W.E., DeBuc, D.C.: Real-time automatic segmentation of optical coherence tomography volume data of the macular region. PLoS ONE **10**(8), 1–20 (2015). https://doi.org/10.1371/journal.pone.0133908
25. Tizhoosh, H.R., Krell, G., Michaelis, B.: Locally adaptive fuzzy image enhancement. In: Reusch, B. (ed.) Fuzzy Days 1997. LNCS, vol. 1226, pp. 272–276. Springer, Heidelberg (1997). https://doi.org/10.1007/3-540-62868-1_118
26. Wang, C., Kaba, D., Li, Y.: Level set segmentation of optic discs from retinal images. J. Med. Syst. **4**(3), 213–220 (2015)
27. Zhang, Y.-J. (ed.): ICIG 2015. LNCS, vol. 9217. Springer, Cham (2015). https://doi.org/10.1007/978-3-319-21978-3
28. Wang, C., Wang, Y., Li, Y.: Automatic choroidal layer segmentation using Markov random field and level set method. IEEE J. Biomed. Health Inform. **21**, 1694–1702 (2017)
29. Yuan, J., Bae, E., Tai, X.C., Boykov, Y.: A study on continuous max- flow and min-cut approaches. In: 2010 IEEE Conference, vo. 7, pp. 2217–2224 (2010)